Supplementary Information for

Rare-metal-free broadband near-infrared phosphors

Guojun Zheng[1,2†], Chenjie Lou[3†], Zeyue Yuan[4,5†], Wenge Xiao[1†*], Longbing Shang[4,5], Jiyou Zhong[6], Mingxue Tang[3*], Jianrong Qiu[2*]

[1]Institute of Light+X Science and Technology, College of Information Science and Engineering, Ningbo University, Ningbo, 315211, China

[2]College of Optical Science and Engineering, Zhejiang University, Hangzhou, 310027, China

[3]Center for High Pressure Science and Technology Advanced Research, Beijing, 100193, China

[4]CAS Key Laboratory of Microscale Magnetic Resonance, School of Physical Sciences, University of Science and Technology of China, Hefei 230026, China

[5]CAS Center for Excellence in Quantum Information and Quantum Physics, University of Science and Technology of China, Hefei 230026, China

[6]School of Physics and Optoelectronic Engineering, Guangdong University of Technology, Guangzhou, 510006, China

[†]These authors contributed equally to this work.

[*] **Corresponding Author:**

Wenge Xiao: xiaowenge@nbu.edu.cn; Mingxue Tang: mingxue.tang@hpstar.ac.cn; Jianrong Qiu: qjr@zju.edu.cn.

This PDF file includes:

Supplementary Figures 1−25

Supplementary Tables 1−23

References 1−15

Supplementary Figures

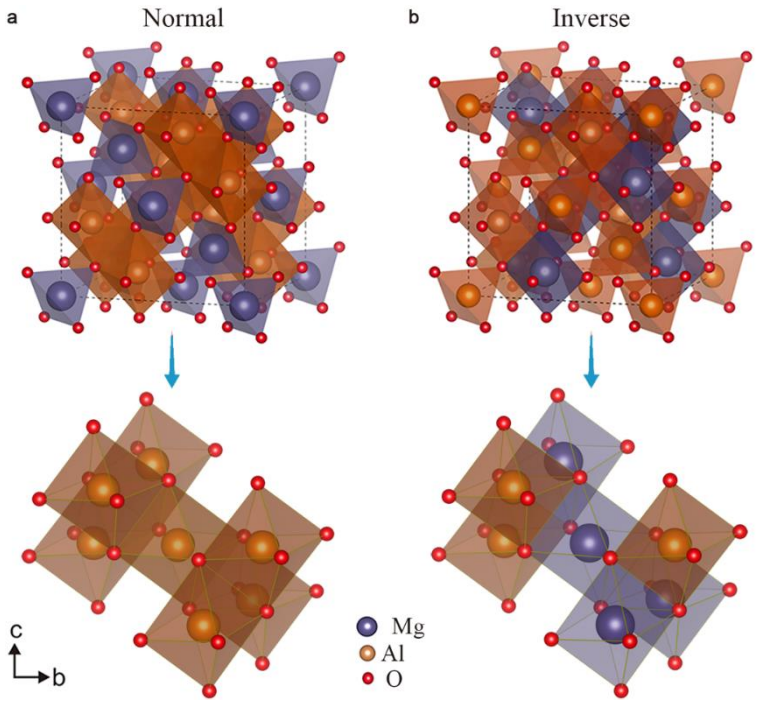

Supplementary Fig. 1 The ground state atomic configurations of normal and inverse spinel structures exemplified by MAS. In the normal spinel structure (**a**), all Al^{3+} ions are in octahedral coordination with D_{3d} symmetry, and all Mg^{2+} ions are in tetrahedral coordination with T_d symmetry. The general formula may be written as $(Mg)[Al]_2O_4$ or $(Mg)_8[Al]_{16}O_{32}$ for the cubic cell, where ( ) and [ ] denote tetrahedral and octahedral sites, respectively. There is such a possible configuration where Mg and Al atoms achieve a completely random distribution in octahedral sites, which can be expressed as $(Al)[MgAl]O_4$ and is so-called inverse spinel structure (**b**).

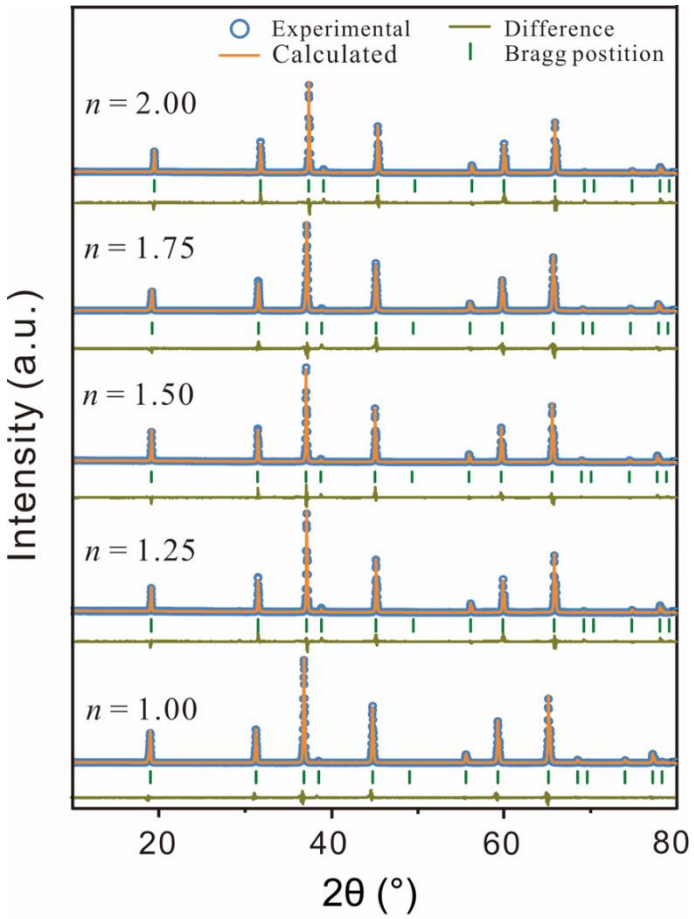

Supplementary Fig. 2 XRD refinements for MA_nS:2.0%Cr^{3+} with varying Al_2O_3 contents.

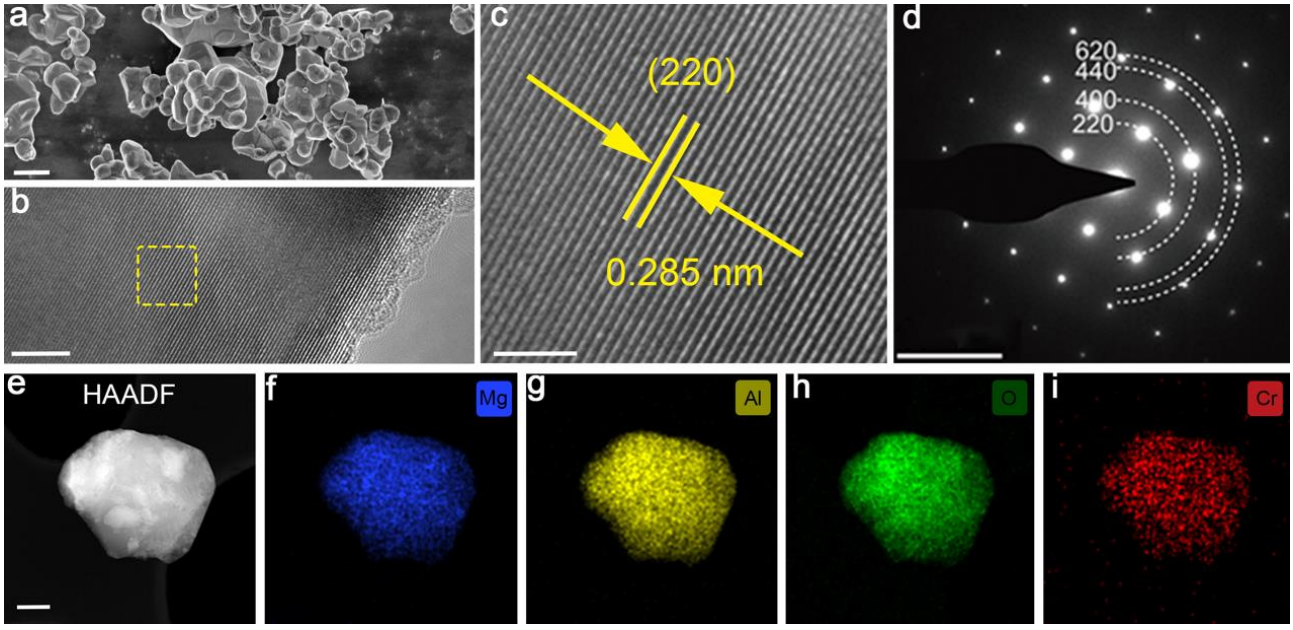

Supplementary Fig. 3 Microstructure characterizations of MAS:2.0%Cr^{3+}. a, SEM image (Scale bar, 1 μm). **b**,**c**, High-resolution TEM images (Scale bar, 5 nm). **d**, Selected area electron diffraction (SAED) patterns (Scale bar, 0.1 nm). **e**, STEM-high angle angular dark field (STEM-HADDF) image. **f**–**i**, EDS mapping images (Scale bar, 200 nm) indicating a uniform distribution of the compositional elements.

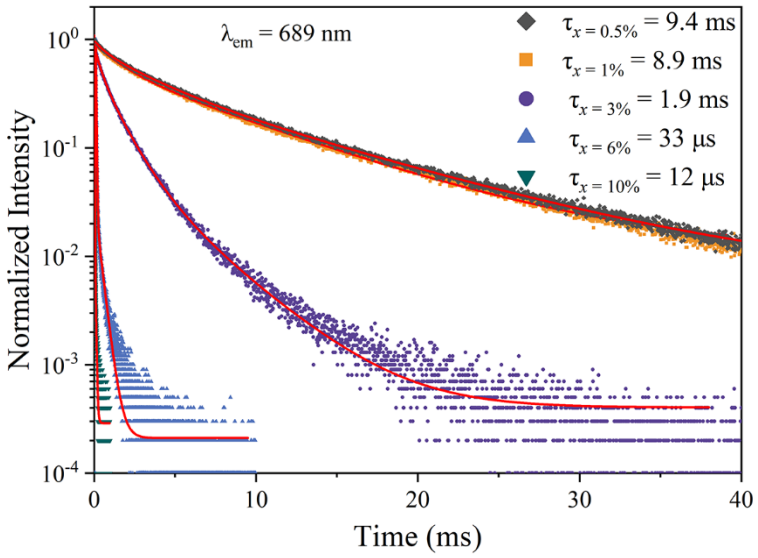

Supplementary Fig. 4 The PL decay curves of MAS:*x*%Cr^{3+} (*x* = 0.5, 1.0, 3.0, 6.0, and 10.0). The PL decay curves were recorded by monitoring the emission at 689 nm. The fitting details are given in Supplementary Table 3. With increasing the Cr^{3+} concentration, the PL decays of the strong-field Cr^{3+} centers ($^2E \rightarrow {}^4A_2$) become faster with the average lifetime calculated decreasing from 9.4 ms for *x* = 0.5% to 1.9 ms for *x* = 3.0%, which confirms the efficient nonradiative energy transfer. Note that the very fast part (dozens of microseconds in average lifetime) in the decay curves for *x* = 6.0% and 10.0% are mainly due to the detected emission from $^4T_2 \rightarrow {}^4A_2$ transitions, since broadband NIR emission becomes dominant at these high concentrations.

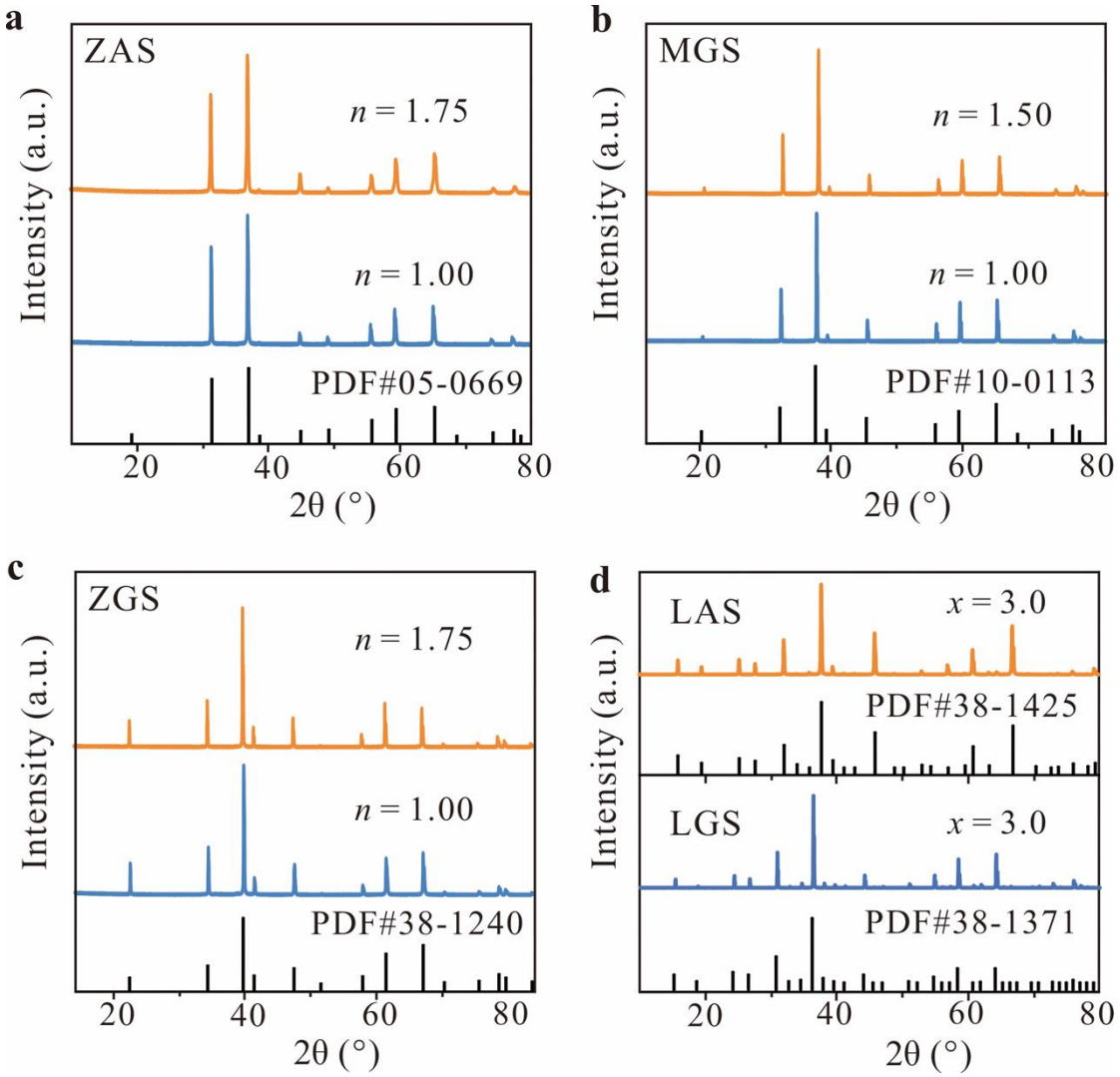

Supplementary Fig. 5 XRD patterns of several representative spinel phosphors. a, ZAS. **b**, MGS. **c**, ZGS. **d,** LAS and LGS. All of the stoichiometric and non-stoichiometric samples have pure spinel phase with XRD patterns matching well with the standard ones.

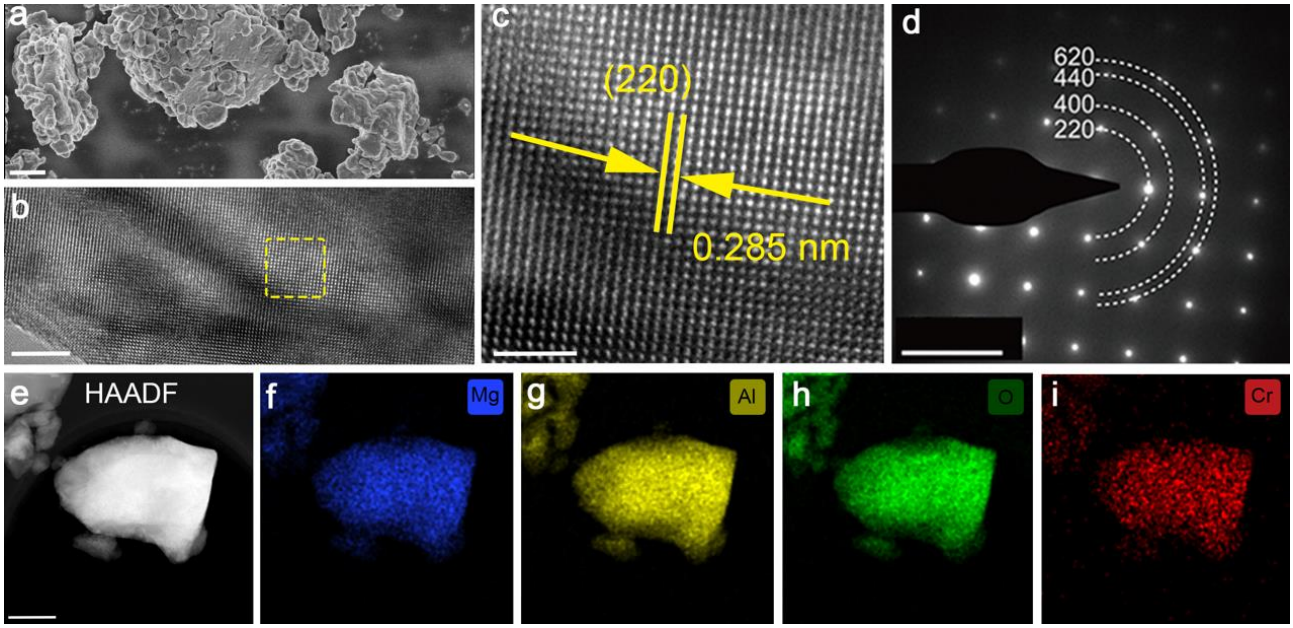

Supplementary Fig. 6 Microstructure characterizations of $MA_{1.75}S$:2.0%Cr^{3+}. a, SEM image (Scale bar, 1 μm). **b**,**c**, High-resolution TEM images (Scale bar, 5 nm). **d**, SAED patterns (Scale bar, 0.1 nm). **e**, STEM-HADDF image. **f**–**i**, EDS mapping images (Scale bar, 200 nm) indicating a uniform distribution of the compositional elements.

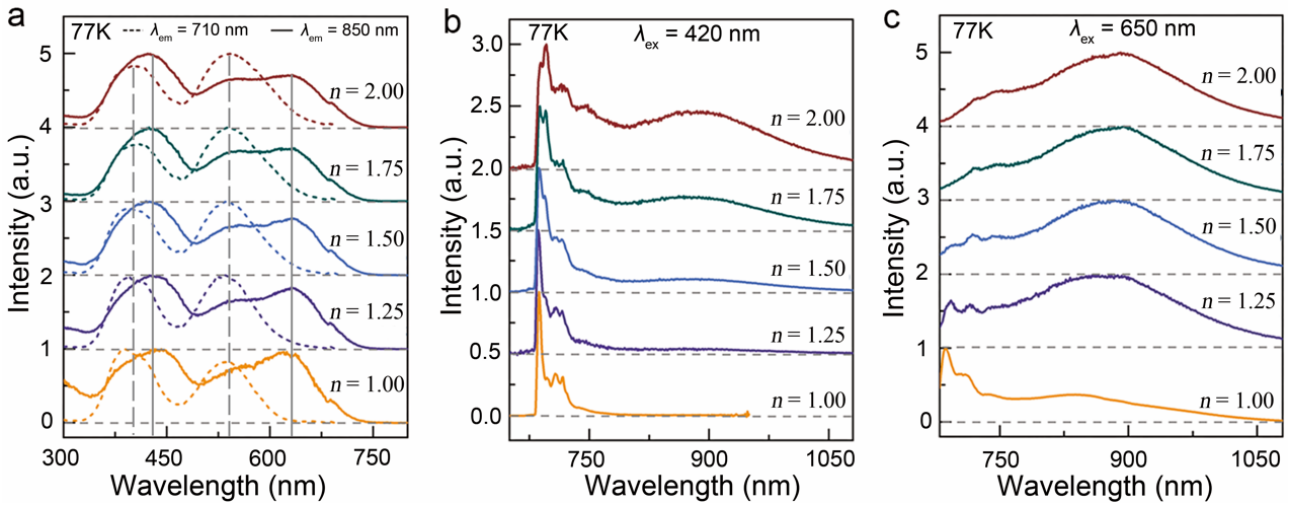

Supplementary Fig. 7 Normalized PLE and PL spectra of MA_nS:0.5%Cr^{3+} at 77 K. **a**, PLE spectra monitoring 710 nm (dash lines) and 850 nm (solid lines). **b**, PL spectra under 420 nm excitation. **c**, PL spectra under 650 nm excitation. With increasing the Al_2O_3 content, the broadband NIR emission around 850 nm is gradually enhanced, indicating that the broadening of PL spectra arises from the increased PL intensity of broadband NIR-emitting Cr^{3+} centers, rather than a gradual redshift of far-red-emitting Cr^{3+} centers induced by the change of crystal field strength at octahedral Al^{3+} sites. When the 650 nm light was used to selectively excite the broadband NIR-emitting Cr^{3+} centers, the above phenomenon becomes more pronounced.

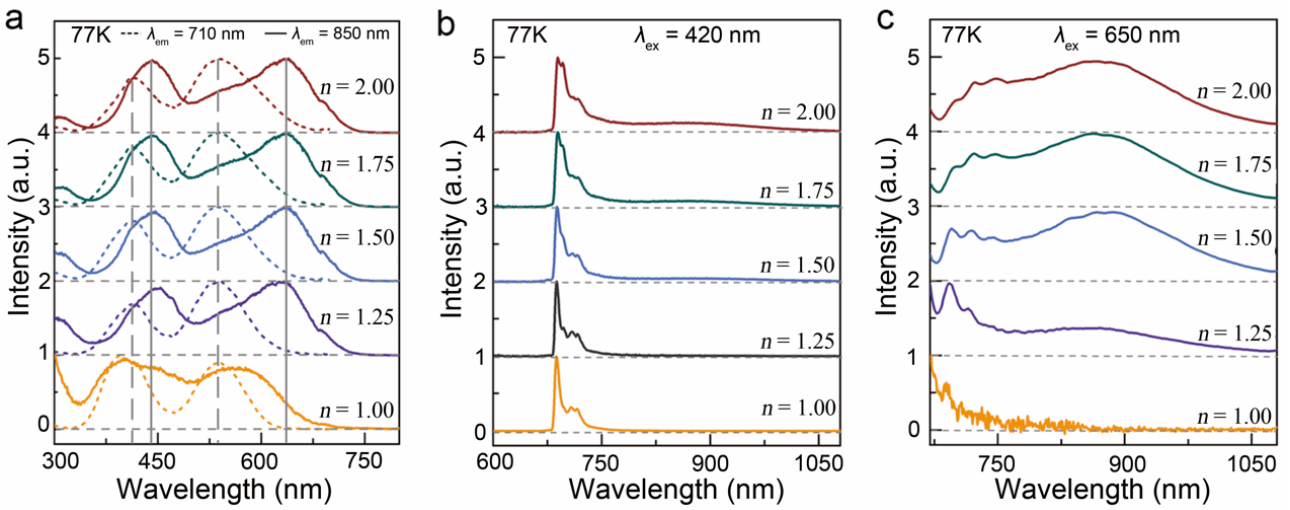

Supplementary Fig. 8 Normalized PLE and PL spectra of MA_nS:0.1%Cr^{3+} at 77 K. **a**, PLE spectra monitoring 710 nm (dash lines) and 850 nm (solid lines). **b**, PL spectra under 420 nm excitation. **c**, PL spectra under 650 nm excitation. Even at such a low Cr^{3+} concentration, the broadband NIR emission can be clearly observed. The crystal field strength (Supplementary Table 8) characterized by the *Dq*/*B* ratio was calculated using the spectroscopic data extracted from these spectra.

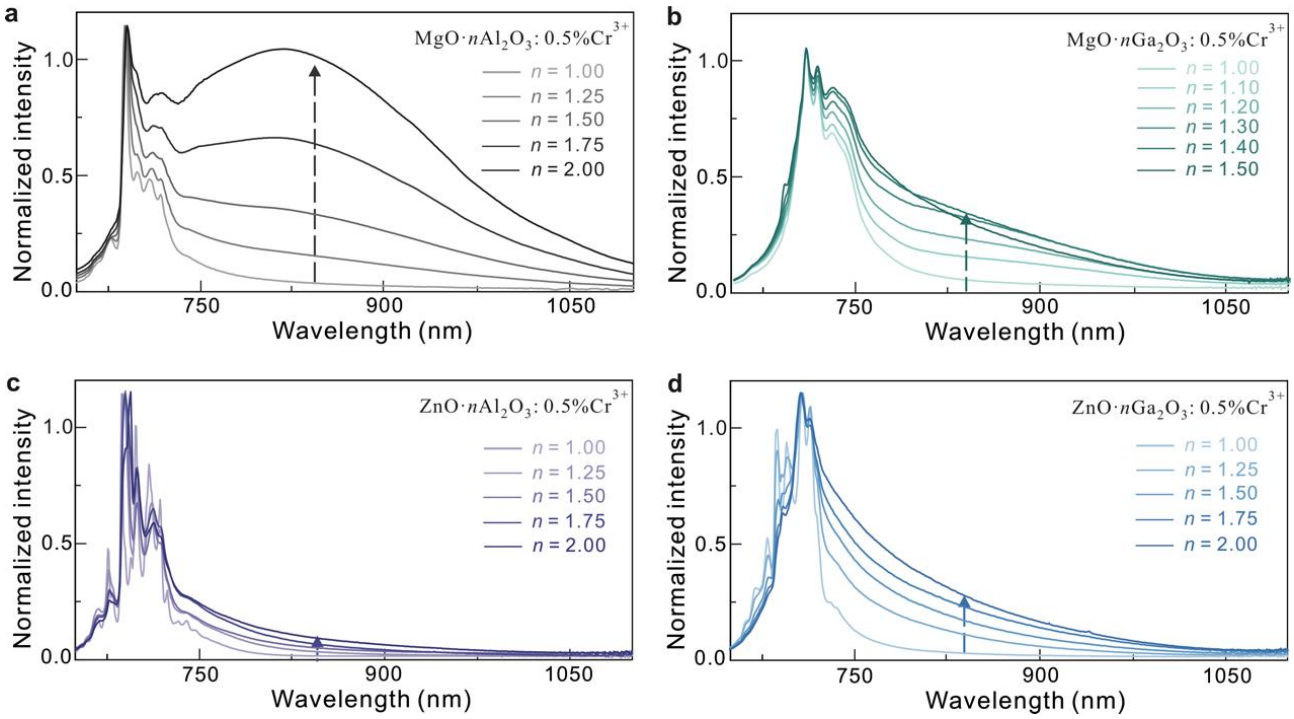

Supplementary Fig. 9 Normalized PL spectra under 420 nm excitation of Cr^{3+} doped spinel phosphors with excess Al_2O_3/Ga_2O_3. a, $MA_nS:0.5\%Cr^{3+}$. **b**, $MG_nS:0.5\%Cr^{3+}$. **c**, $ZA_nS:0.5\%Cr^{3+}$. **d**, $ZG_nS:0.5\%Cr^{3+}$.

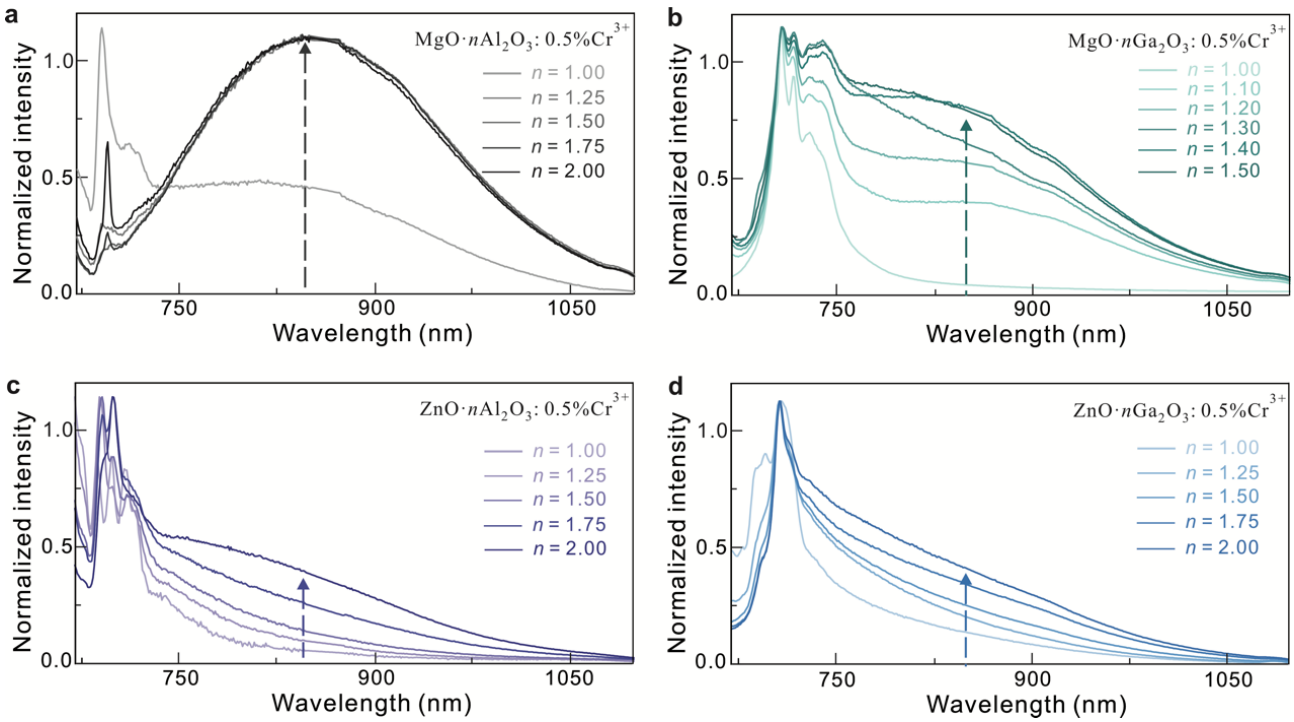

Supplementary Fig. 10 Normalized PL spectra under 650 nm excitation of Cr^{3+} doped spinel phosphors with excess Al_2O_3/Ga_2O_3. a, $MA_nS:0.5\%Cr^{3+}$. **b**, $MG_nS:0.5\%Cr^{3+}$. **c**, $ZA_nS:0.5\%Cr^{3+}$. **d**, $ZG_nS:0.5\%Cr^{3+}$. When the 650 nm light was used to selectively excite the broadband NIR-emitting Cr^{3+} centers, the spectral changes become more pronounced.

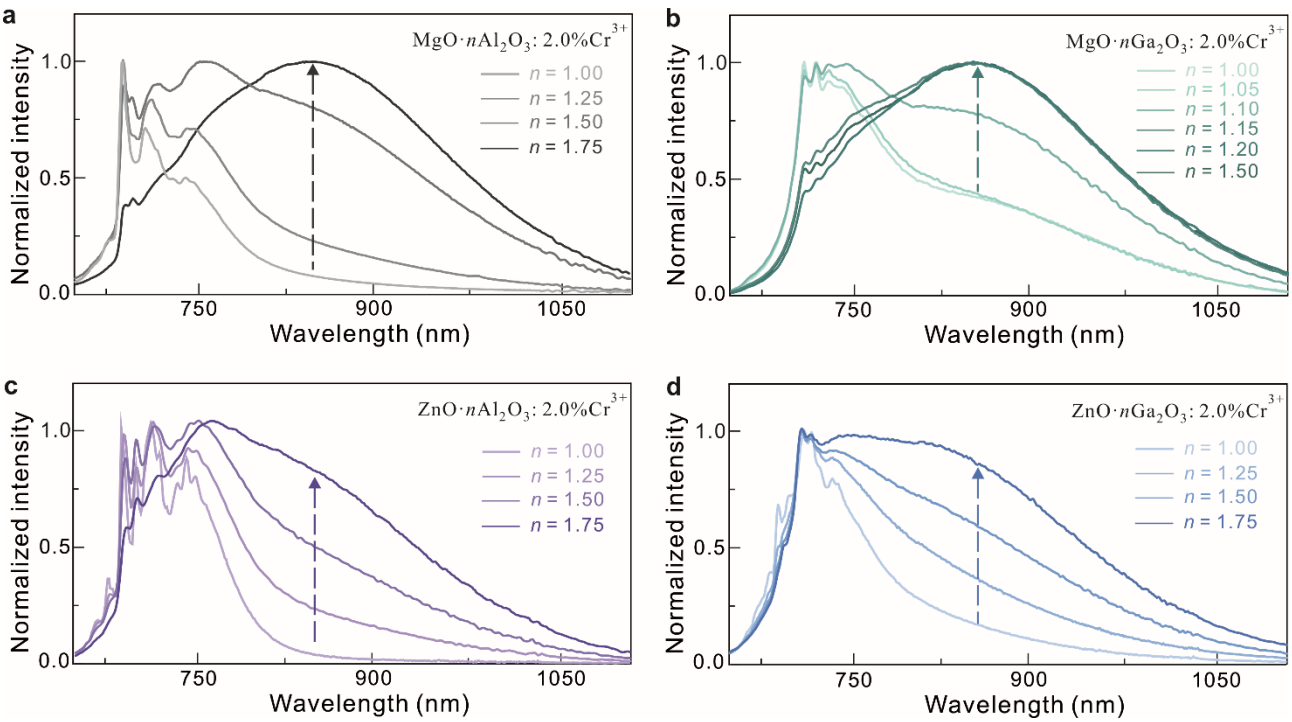

Supplementary Fig. 11 Normalized PL spectra under 450 nm excitation of Cr^{3+} doped spinel phosphors with excess Al_2O_3/Ga_2O_3. a, $MA_nS:2.0\%Cr^{3+}$. **b**, $MG_nS:2.0\%Cr^{3+}$. **c**, $ZA_nS:2.0\%Cr^{3+}$. **d,** $ZG_nS:2.0\%Cr^{3+}$.

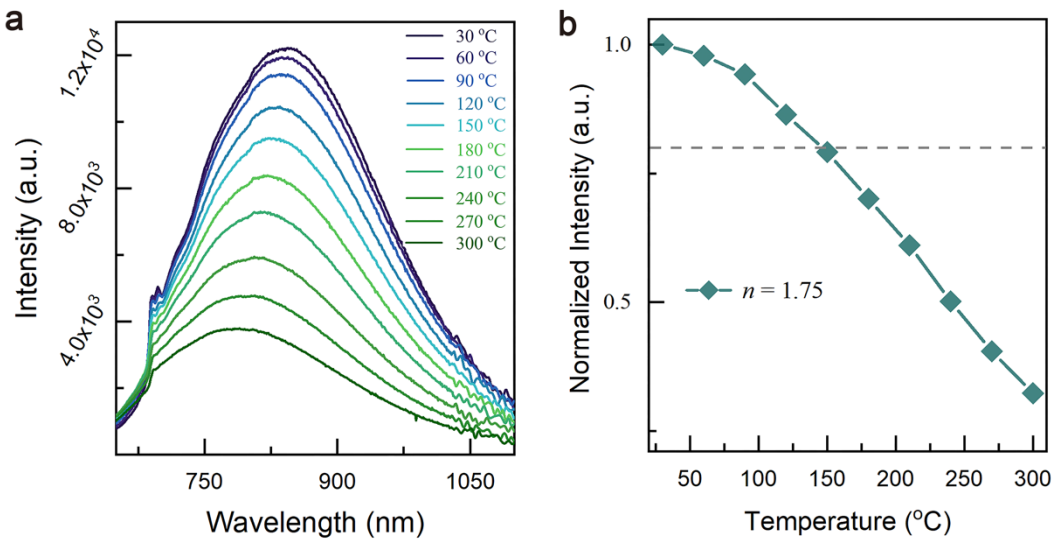

Supplementary Fig. 12 Temperature-dependent PL properties of $MA_{1.75}S$:2.0%Cr^{3+}. a, Temperature-dependent PL spectra. **b**, Integrated PL intensities as a function of the temperature. The PL intensity at 150 °C is as high as 80% of that at room temperature, indicating a weak thermal quenching.

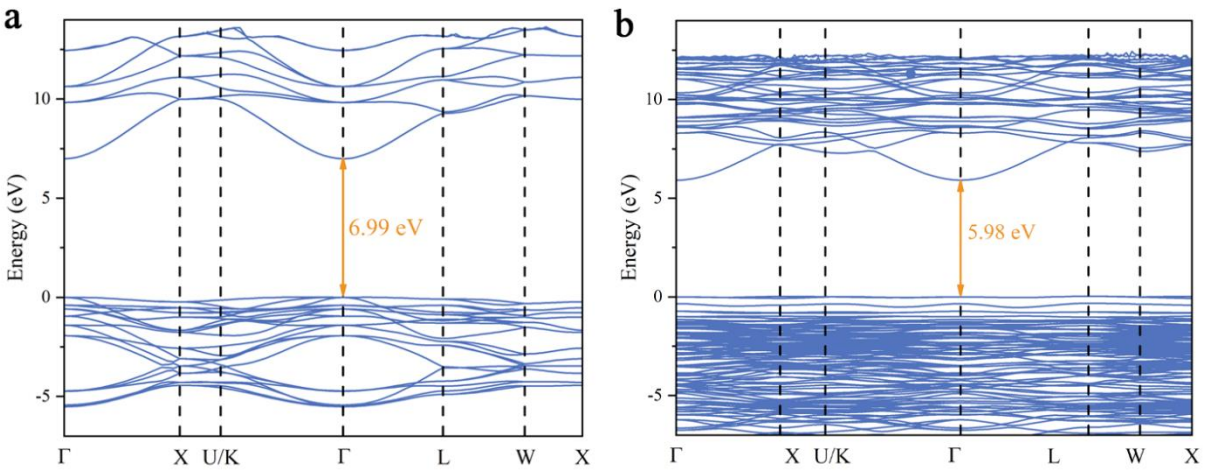

Supplementary Fig. 13 The electronic band structures of $MgAl_2O_4$ and $Mg_5Al_{18}O_{32}$ (representing $MA_{1.75}S$) along high symmetric K-points Γ–X–U/K–Γ–L–W–X. The band gaps of MAS and $MA_{1.75}S$ are calculated to be 6.99 and 5.98 eV, respectively, which are consistent with previous work (ACS Org. Inorg. Au 2024, 4, 120); the smaller band gap for $MA_{1.75}S$ is mainly due to the cation vacancies located at the octahedral positions (J. Am. Ceram. Soc., 1997, 80, 1193). Their real values should be a little higher; for example, the band gap of MAS is experimentally determined to be 7.80−8.10 eV (Geochimica et Cosmochimica Acta, 1974, 38, 589; ACS Org. Inorg. Au 2024, 4, 120).

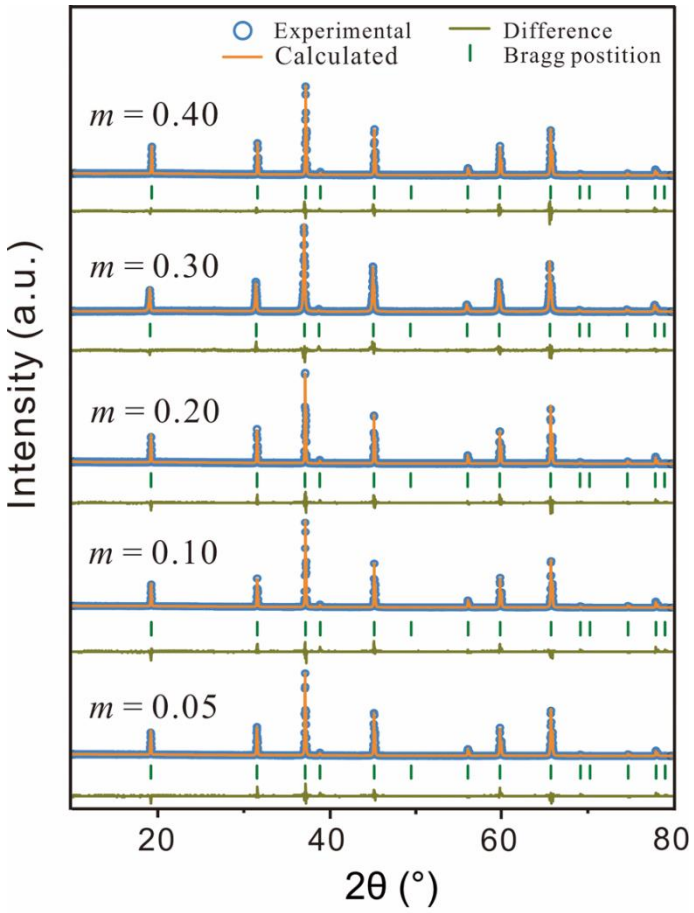

Supplementary Fig. 14 XRD refinements for $MA_{1.75}S$:2.0%Cr^{3+},*m*Si.

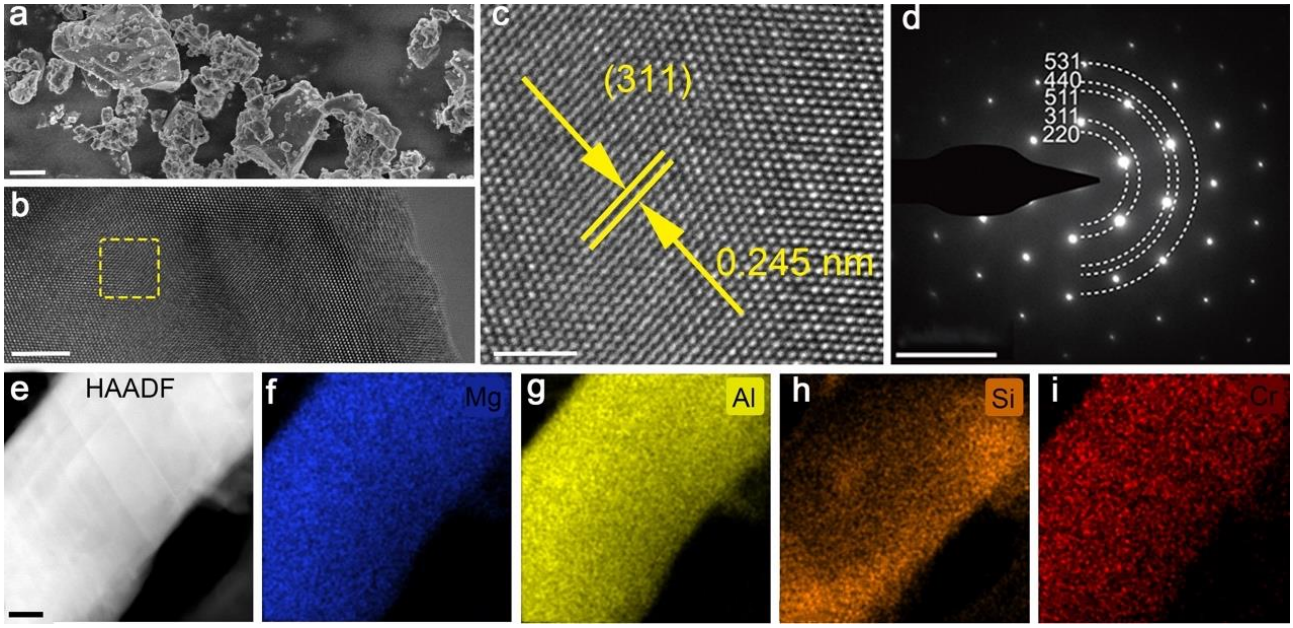

Supplementary Fig. 15 Microstructure characterizations of $MA_{1.75}S$:2.0%Cr^{3+},0.30Si. a, SEM image (Scale bar, 1 μm). **b**,**c**, High-resolution TEM images (Scale bar, 5 nm). **d**, SAED patterns (Scale bar, 0.1 nm). **e**, STEM-HADDF image. **f**–**i**, EDS mapping images (Scale bar, 200 nm) indicating a uniform distribution of the compositional elements.

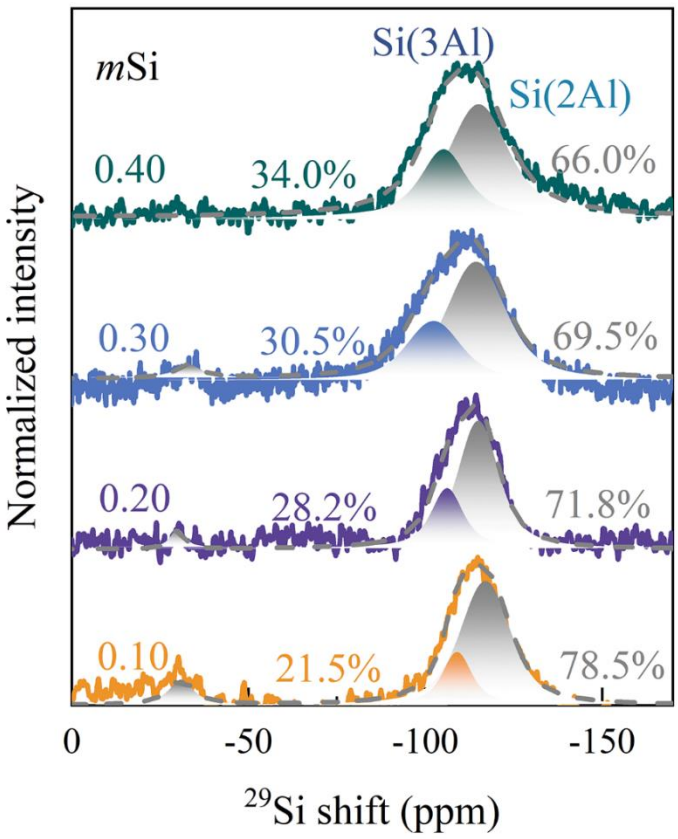

Supplementary Fig. 16 ^{29}Si NMR spectra for MA$_{1.75}$S:2.0%Cr^{3+},*m*Si. The solid lines are the measured data and the dashed lines are the total simulations. The assignments and the corresponding calculated occupancies are given next to each component. The results indicate that Si^{4+} ions exclusively enter tetrahedral sites.

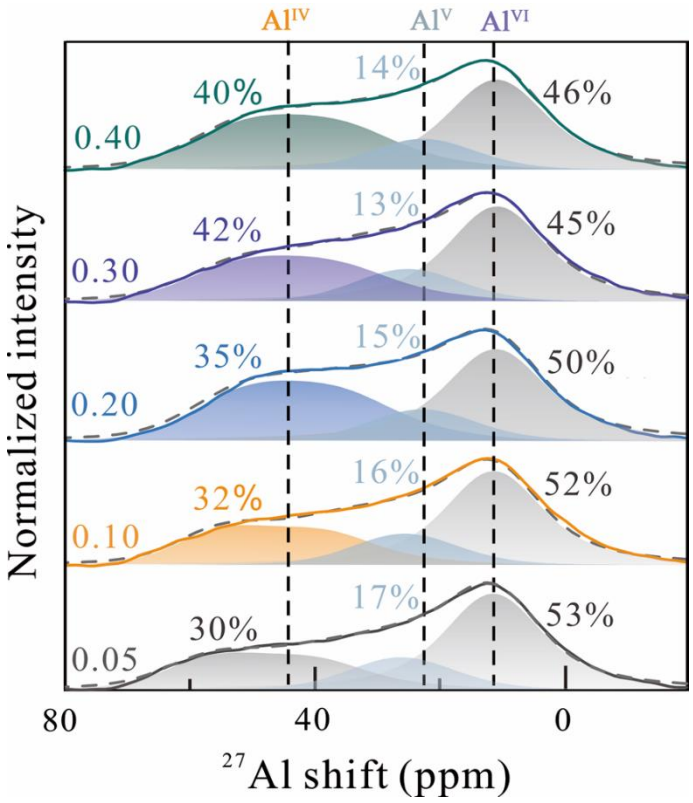

Supplementary Fig. 17 ^{27}Al MAS NMR spectra of MA$_{1.75}$S:2.0%Cr^{3+},*m*Si. The solid lines are measured data and the dashed lines are the total simulated spectra. The calculated occupancies are given next to each component.

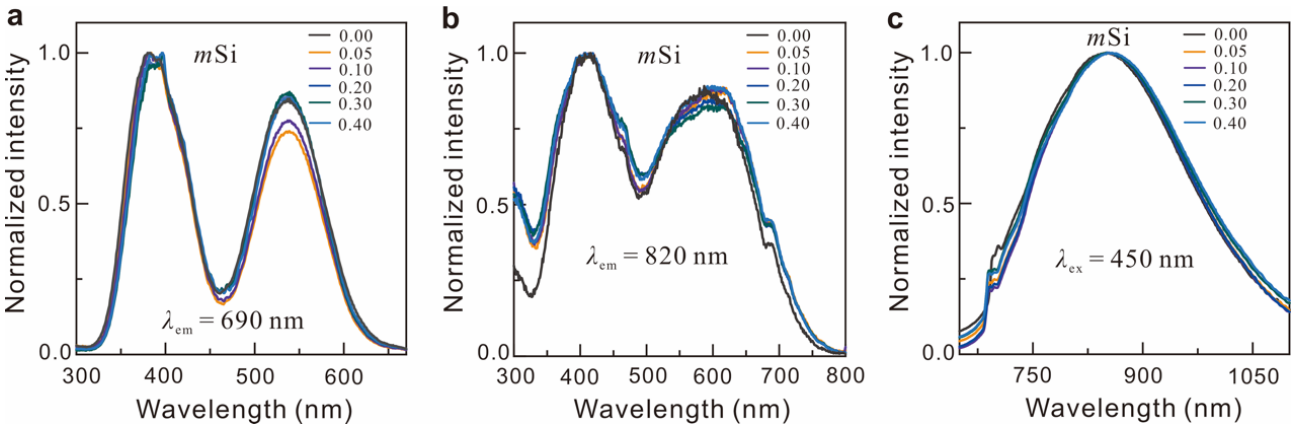

Supplementary Fig. 18 PLE and PL spectra of $MA_{1.75}S$:2.0%Cr^{3+},*m*Si. a,**b**, Normalized PLE spectra monitoring 690 nm (**a**) and 820 nm (**b**). **c**, Normalized PL spectra under 450 nm excitation. The substitution of smaller Si^{4+} for larger Al^{3+} would lead to a blueshift in PL spectra according to the crystal field theory; the very small redshift observed here indicates that more weak-field Cr^{3+} centers are formed due to the increased cation inversion.

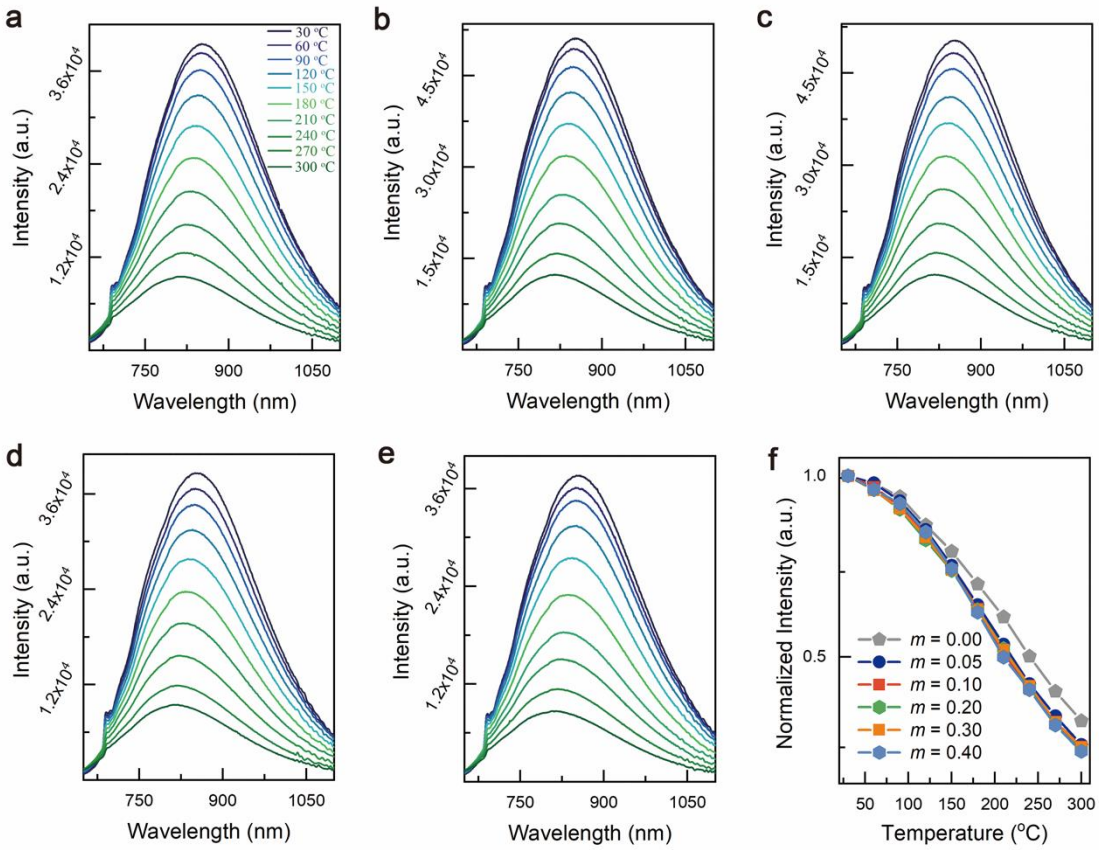

Supplementary Fig. 19 Temperature-dependent PL properties of $MA_{1.75}S$:2.0%Cr^{3+},*m*Si. a–e, Temperature-dependent spectra upon 450 nm excitation. **f**, Integrated PL intensities as a function of the temperature. The PL intensity for all the Si-substituted samples at 150 °C is as high as 77% of that at room temperature.

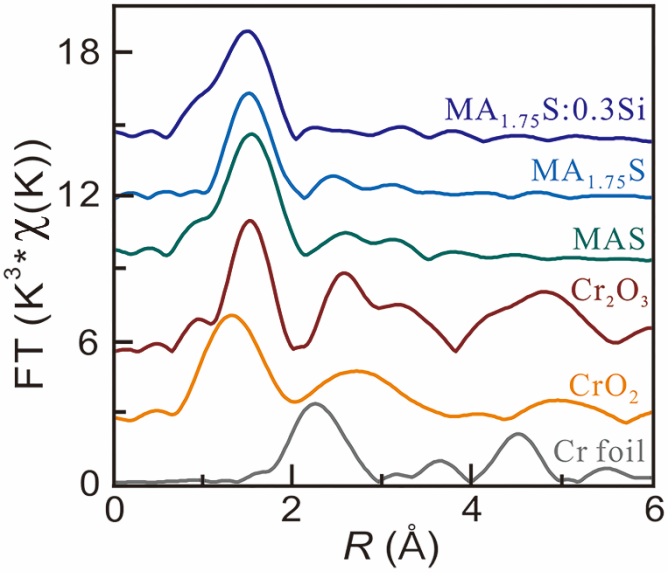

Supplementary Fig. 20 The k^3 weighted forward Fourier transformed EXAFS spectra in *R* space of Cr^{3+} for three representative samples and the standard samples.

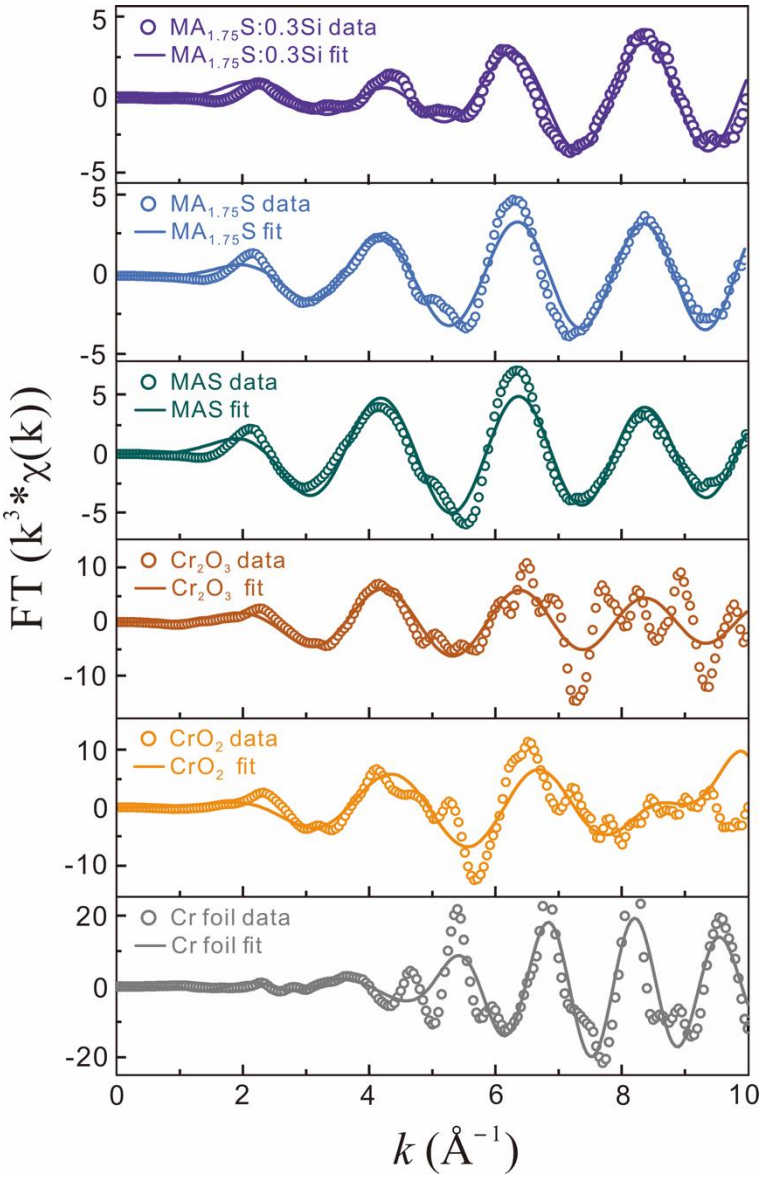

Supplementary Fig. 21 The k^3-weighted EXAFS data in k space. The k^3 weighting, k-range of 0–10.0 $Å^{-1}$ and R range of ~1.0–3.0 Å were used for the fitting. The fitting results coincide with the measured ones very well, indicating that the data is reliable.

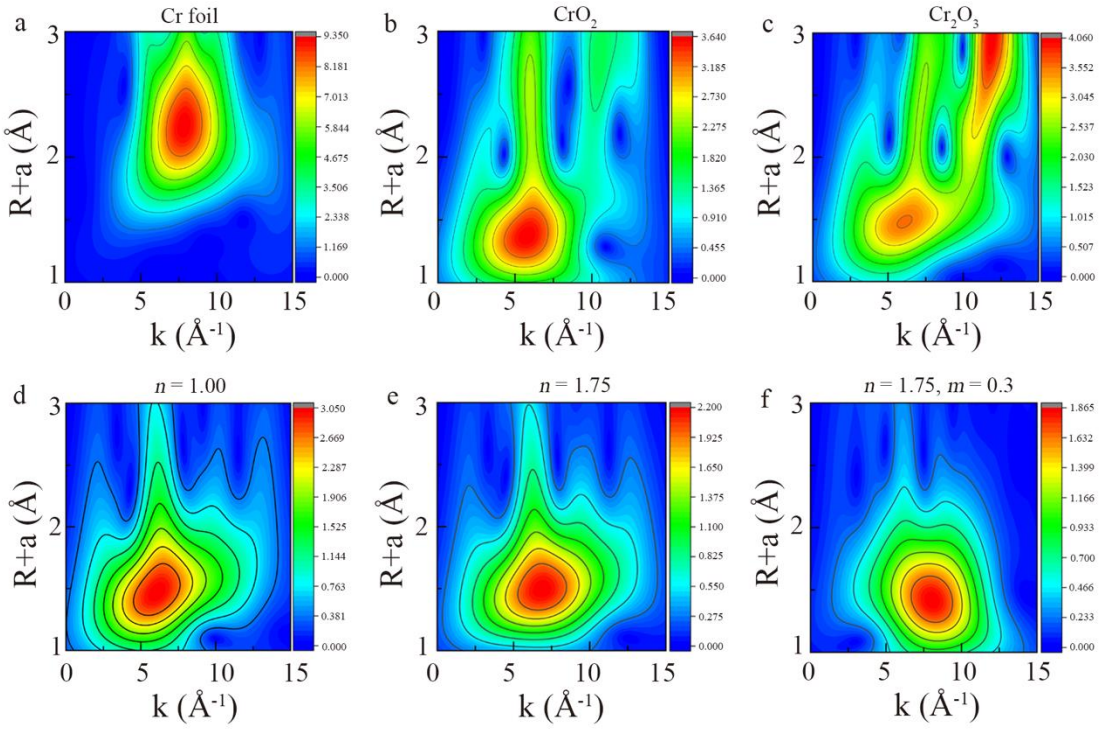

Supplementary Fig. 22 Wavelet transforms for the k^3-weighted Cr *K*-edge EXAFS signals. a–**c**, The standard samples**. d**–**f**, Three representative samples, MAS:2%Cr^{3+} (**d**) $MA_{1.75}$S:2%Cr^{3+} (**e**) and $MA_{1.75}$S:2%Cr^{3+},0.3Si (**f**). For Wavelet Transform analysis, the χ (*k*) exported from Athena was imported into the Hama Fortran code (Phys. Rev. B 71, 094110 (2005)). The parameters were listed as follow: *R* range, 1–3.0 Å, *k* range, 0–15$Å^{-1}$; *k* weight, 3; and Morlet function with κ = 5, σ = 1 was used as the mother wavelet to provide the overall distribution.

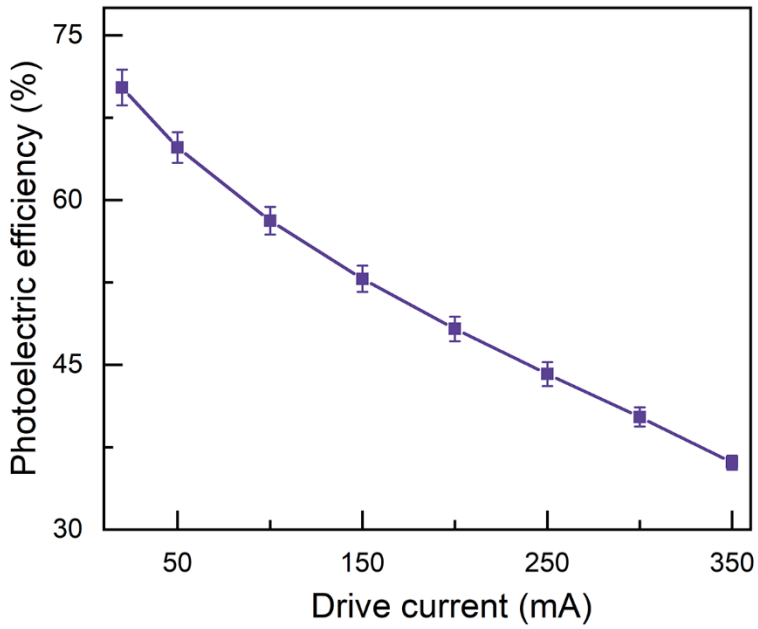

Supplementary Fig. 23 The photoelectric efficiency of 450 nm LED chips as a function of driving current. Error bars represent the range of efficiency values after measuring five different LED chips.

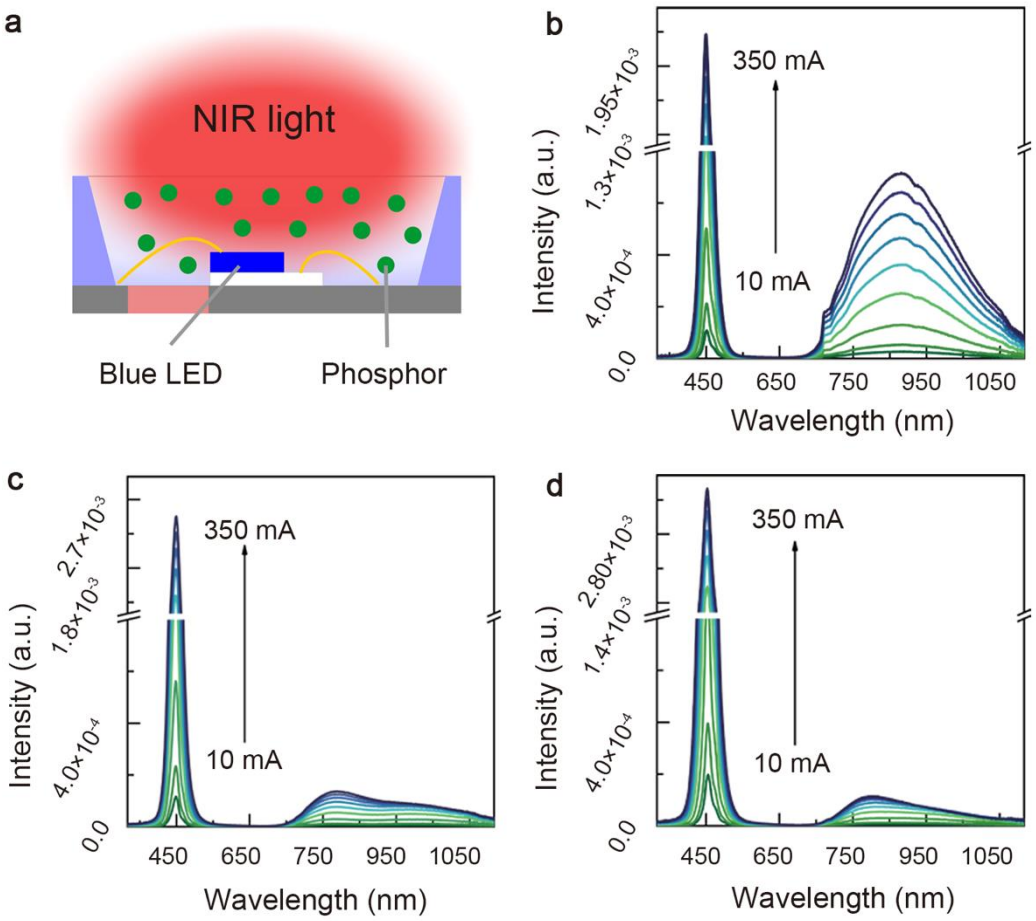

Supplementary Fig. 24 Fabrication and characterization of NIR pc-LEDs. a, Schematic of NIR pc-LED. **b**–**d**, EL spectra of pc-LED devices under different drive currents, including the as-fabricated pc-LED (**b**), SFH 4737 (**c**) and LUXEON IR ONYX (**d**).

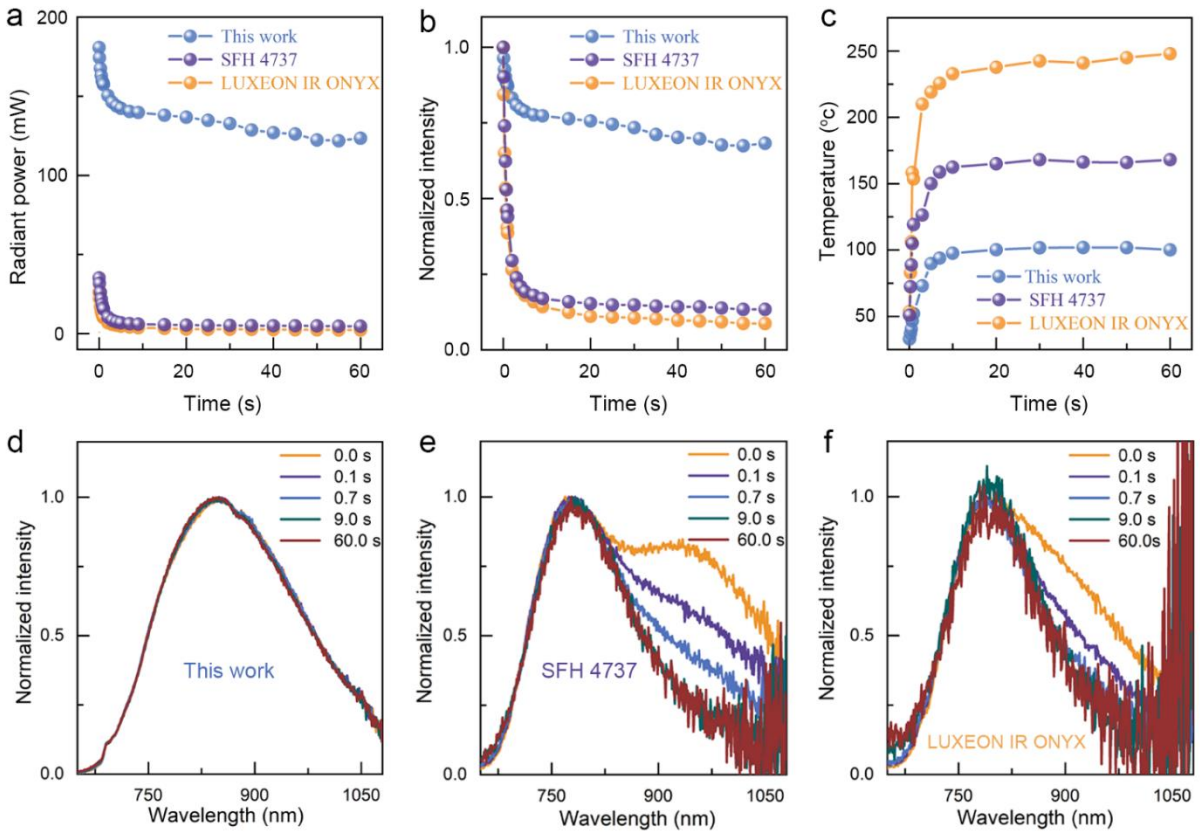

Supplementary Fig. 25 Lighting-time-dependent photoelectric properties of NIR pc-LEDs at a fixed current of 350 mA. a,**b** The absolute (**a**) and normalized (**b**) NIR optical power of the as-fabricated pc-LED and two commercial products measured after lighting for varying times. **c**, The surface temperature of the devices. **d**,**e**,**f**, The normalized EL spectra of our work (**d**), SFH 4737 (**e**) and LUXEON IR ONYX (**f**) after different lighting times. Note that we did not use any thermal conductors to dissipate the heat generated by the pc-LED devices so that the rise of temperatures can be accelerated. All these devices show a reduction in NIR optical power/photoelectric efficiency with increasing the lighting time (t), especially when t < 10 s; accordingly, their operating temperatures show a gradual increase, and a much faster increase when t < 10 s. Notably, when the thermal equilibrium is achieved at t > 20 s, the corresponding temperature is much smaller for our device, which is mainly due to the high photoelectric efficiency; the relative decrements (compared with that at t = 0 s) of the NIR optical power/photoelectric efficiency are also smaller for our device; besides, similar to the current-dependent EL spectra (Fig. 4c in the manuscript), the time-dependent EL spectra of our device operated at 350 mA show negligible change in profile, whereas for the commercial ones, the relative EL intensity of the long-wavelength emission decreases clearly. These

results undoubtedly confirm the superior thermal stability as well as the high conversion efficiency of the developed phosphor.

Supplementary Tables

Table S1 Details of Rietveld refinement crystallographic data for MA_nS:2.0%Cr^{3+}.

Crystallogtaphic Data					
n	1.00	1.25	1.50	1.75	2.00
Lattice parameter, *a* (Å)	8.089377(17)	8.065470(15)	8.043050(19)	8.027517(19)	8.015018(24)
Volume(Å^3)	529.3529(33)	524.6733(30)	520.3102(36)	517.3015(37)	514.8890(47)
R_{wp}	5.76%	5.16%	4.87%	5.26%	5.70%
R_p	4.20%	3.87%	3.51%	3.57%	3.93%
Gof	2.43	2.17	2.04	2.23	1.95
Site occupancy fractions:					
Mg(1/8,1/8,1/8)	0.584	0.522	0.388	0.294	0.270
Al(1/8,1/8,1/8)	0.416	0.478	0.612	0.706	0.730
Mg(1/2,1/2,1/2)	0.208	0.289	0.306	0.352	0.364
Al(1/2,1/2,1/2)	0.792	0.711	0.694	0.647	0.635
Cr(1/2, 1/2, 1/2)	0.010	0.010	0.010	0.010	0.010
Isotropic temperature factor, Biso:					
Mg/Al(1/8,1/8,1/8)	1.050(36)	1.263(34)	0.674(33)	0.907(35)	0.716(37)
Al/Mg(1/2,1/2,1/2)	0.731(29)	0.802(30)	1.342(41)	1.538(46)	1.699(48)
O (*u*, *u*, *u*)	0.618(61)	0.200(61)	0.200(84)	0.200(93)	0.200(93)

Table S2 EDS results of MAS:2.0%Cr^{3+}, $MA_{1.75}$S:2.0%Cr^{3+}, and $MA_{1.75}$S:2.0%Cr^{3+}, 0.30Si.

Samples	Elements	Atomic Fraction	Errors
MAS:2.0%Cr^{3+}	Mg	13.76%	3.28%
	Al	28.89%	6.86%
	O	56.52%	7.44%
	Cr	0.82%	0.15%
$MA_{1.75}$S:2.0%Cr^{3+}	Mg	9.57%	2.33%
	Al	33.12%	8.06%
	O	56.51%	8.04%
	Cr	0.80%	0.16%
$MA_{1.75}$S:2.0%Cr^{3+}, 0.30Si	Mg	8.19%	1.88%
	Al	26.29%	6.03%
	Si	3.32%	0.75%
	O	61.67%	7.23%
	Cr	0.53%	0.09%

Table S3 The fitting parameters of PL decay curves for MAS:*x*%Cr^{3+} monitoring 689 nm.

x%	A_1	τ_1	A_2	τ_2	A_3	τ_3	I_0	R^2
0.5	0.21	1.24	0.47	4.93	0.26	13.12	8.98×10^{-5}	0.99965
1.0	0.17	0.67	0.46	3.74	0.31	11.69	0.01×10^{-6}	0.99962
3.0	0.24	0.36	0.47	1.24	0.09	3.43	4.02×10^{-4}	0.99964
6.0	61.63	0.03	0.10	0.13	0.01	0.77	9.07×10^{-5}	0.99942
10.0	0.46	0.01	2.98	0.01	0.03	0.05	2.90×10^{-4}	0.99768

The PL decay curves were best fitted to triple-exponential functions, which could be described by the following equation:

$$I(t) = A_1 \exp\left(-\frac{t}{\tau_1}\right) + A_2 \exp\left(-\frac{t}{\tau_2}\right) + A_3 \exp\left(-\frac{t}{\tau_3}\right) + I_0 \quad (1)$$

According to eqn (1), the average lifetime τ_{ave} is given by:

$$\tau_{ave} = \frac{A_1\tau_1^2 + A_2\tau_2^2 + A_3\tau_3^2}{A_1\tau_1 + A_2\tau_2 + A_3\tau_3} \quad (2)$$

According to eqn (2), the average lifetimes of the 689 nm luminescence were calculated and given in Supplementary Fig. 4.

Table S4 IQE, AE, and EQE values of MAS:*x*%Cr^{3+}.

x	IQE (%)	AE (%)	EQE (%)
1	98	19	19
3	79	34	27
6	47	40	19
10	27	44	12

Table S5 IQE, AE, and EQE values of ZAS:*x*%Cr^{3+}.

x	IQE (%)	AE (%)	EQE (%)
1	98	20	20
3	90	33	30
6	14	39	5
10	10	43	4

Table S6 IQE, AE, and EQE values of LAS:*x*%Cr^{3+}.

x	IQE (%)	AE (%)	EQE (%)
0.5	81	27	22
1.0	76	30	23
3.0	70	41	29
5.0	39	46	18

Table S7 IQE, AE, and EQE values of MGS:*x*%Cr^{3+}.

x	IQE (%)	AE (%)	EQE (%)
1	98	34	33
3	82	46	38
6	41	50	21
10	14	52	7

Table S8 IQE, AE, and EQE values of ZGS:*x*%Cr^{3+}.

x	IQE (%)	AE (%)	EQE (%)
1	97	33	32
3	78	43	34
6	12	47	6
10	1	49	1

Table S9 IQE, AE, and EQE values of LGS:*x*%Cr^{3+}.

x	IQE (%)	AE (%)	EQE (%)
0.5	100	31	31
1.0	99	36	36
3.0	88	46	40
5.0	53	52	28

Table S10 Crystal field parameters of Cr^{3+} in $MA_{1.75}S$:0.1%Cr^{3+}.

$E(^4A_2 \rightarrow {}^4T_1)$ (cm^{-1})	$E(^4A_2 \rightarrow {}^4T_2)$ (cm^{-1})	$E(^4T_2 \rightarrow {}^4A_2)$ (cm^{-1})	$E(^2E \rightarrow {}^4A_2)$ (cm^{-1})	ΔE (cm^{-1})	Dq (cm^{-1})	B (cm^{-1})	Dq/B
23255	16129	11627	/	7126	1388	807	1.72
24570	18622	/	14513	5948	1657	577	2.87

The crystal field parameters were calculated by using the following formulas:

$$\Delta E = E(4A2 \rightarrow 4T1) - E(4A2 \rightarrow 4T2) \quad (1)$$

$$\Delta S = E(4A2 \rightarrow 4T2) - E(4T2 \rightarrow 4A2) \quad (2)$$

$$10Dq = E(4A2 \rightarrow 4T2) - \frac{\Delta S}{2} \quad (3)$$

$$\frac{Dq}{B} = \frac{15 \times \left(\frac{\Delta E}{Dq} - 8\right)}{\left(\frac{\Delta E}{Dq}\right)^2 - 10 \times \frac{\Delta E}{Dq}} \quad (4)$$

where Dq is the crystal field strength parameter and B is Racah electron repulsion parameter; the values of $E(^4A_{2g} \rightarrow {}^4T_{1g})$ and $E(^4A_{2g} \rightarrow {}^4T_{2g})$ were calculated from the corresponding peak energy of the PLE band, and ΔE represents the energy difference between the two energy levels $E(^4A_{2g} \rightarrow {}^4T_{1g})$ and $E(^4A_{2g} \rightarrow {}^4T_{2g})$. The Stokes shift ($\Delta S$) was calculated from the peak position of the PLE band corresponding to $E(^4A_{2g} \rightarrow {}^4T_{2g})$ and the peak position in the PL spectrum corresponding to $E(^4T_{2g} \rightarrow {}^4A_{2g})$.

Table S11 IQE, AE, and EQE values of MG_nS:2.0%Cr^{3+}.

n	IQE (%)	AE (%)	EQE (%)
1.00	93	36	33
1.05	95	38	36
1.10	94	40	38
1.15	92	41	38
1.20	91	42	38
1.50	80	44	35

Table S12 IQE, AE, and EQE values of ZG_nS:2.0%Cr^{3+}.

n	IQE (%)	AE (%)	EQE (%)
1.00	92	40	37
1.25	92	41	38
1.50	90	42	38
1.75	93	44	41

Table S13 IQE, AE, and EQE values of ZA_nS:2.0%Cr^{3+}.

n	IQE (%)	AE (%)	EQE (%)
1.00	96	31	30
1.25	84	31	26
1.50	78	33	26
1.75	80	34	27

Table S14 Calculated inversion parameters (*i*) of MA_nS:2.0%Cr^{3+} based on NMR, FTIR, and Raman spectra, respectively.

n	NMR	FTIR	Raman
1.00	0.17	0.19	0.25
1.15	0.22	0.22	0.30
1.50	0.26	0.35	0.31
1.75	0.29	0.39	0.32
2.00	0.31	0.40	0.33

Table S15 IQE, AE, and EQE values of $MA_nS:0.5\%Cr^{3+}$.

n	IQE (%)	AE (%)	EQE (%)
1.00	100	17	17
1.15	99	18	18
1.50	97	21	20
1.75	98	24	24
2.00	91	26	24

Table S16 IQE, AE, and EQE values of $MA_{1.75}S:x\%Cr^{3+}$.

x	IQE (%)	AE (%)	EQE (%)
0.5	98	24	24
1.0	96	31	30
2.0	95	35	33
3.0	82	40	33
6.0	65	49	32
10.0	40	54	22

Table S17. The total elastic moduli (kBar) of MAS:2.0%Cr^{3+} (Θ_D = 804.1 K).

Direction	XX	YY	ZZ	XY	YZ	ZX
XX	2582.9115	1446.9760	1446.9760	0.0000	0.0000	0.0000
YY	1446.9760	2582.9115	1446.9760	0.0000	0.0000	0.0000
ZZ	1446.9760	1446.9760	2582.9115	0.0000	0.0000	0.0000
XY	0.0000	0.0000	0.0000	1285.5422	0.0000	0.0000
YZ	0.0000	0.0000	0.0000	0.0000	1285.5422	0.0000
ZX	0.0000	0.0000	0.0000	0.0000	0.0000	1285.5422

The Perdew–Burke–Ernzerhof (PBE) exchange-correlation functional was employed for stress tensor calculation to estimate the Debye temperature (Θ_D).[76,77] With the calculated elastic constants, it is possible to estimate the Debye temperature using the following equations:

$$\Theta_D = \frac{h}{k}\left(\frac{3n}{4\pi}\frac{N_A\rho}{M}\right)^{\frac{1}{3}} v_m \quad (1)$$

$$v_m = \left[\frac{1}{3}\left(\frac{2}{v_t^3} + \frac{1}{v_l^3}\right)\right]^{-\frac{1}{3}} \quad (2)$$

$$v_l = \sqrt{\frac{3B + 4G}{3\rho}},\ v_t = \sqrt{\frac{G}{\rho}} \quad (3)$$

where h = 6.626×10^{-34} J·s is the Planck's constant; k_B = 1.381×10^{-23} J·K^{-1} is the Boltzmann constant; N_A = 6.022×1023 mol^{-1} is the Avogadro's number; ρ is the crystal's density; n is the number of atoms per one formula unit, and M is the formula weight. The average, transverse and longitudinal sound velocities are denoted by v_m, v_t, v_l, correspondingly. The B (bulk modulus) and G (shear modulus) values are calculated as the average values of the corresponding Voigt and Reuss (denoted with the V and R subscripts, respectively) values from Tables S17, S18 and S21. With these equations and calculated elastic parameters, the Debye temperatures for MAS:2.0%Cr^{3+}, $MA_{3.5}$S:2.0%Cr^{3+}, and $MA_{3.5}$S:2.0%Cr^{3+},0.3Si were estimated to be 804.1 K, 872.8 K, and 833.5 K, respectively.

Table S18. The total elastic moduli (kBar) of $MA_{1.75}S$:2.0%Cr^{3+} (Θ_D = 872.8 K).

Direction	XX	YY	ZZ	XY	YZ	ZX
XX	2866.0089	1366.0795	1364.7012	-3.4731	-15.0543	-5.3017
YY	1366.0795	2850.3892	1367.5904	-2.5211	11.9341	-0.0573
ZZ	1364.7012	1367.5904	2835.7294	-5.0897	19.1466	3.3237
XY	-3.4731	-2.5211	-5.0897	1428.1617	2.7826	19.8723
YZ	-15.0543	11.9341	19.1466	2.7826	1449.1802	19.3426
ZX	-5.3017	-0.0573	3.3237	19.8723	19.3426	1431.6257

Table S19. Details of Rietveld refinement crystallographic data for $MA_{1.75}S$:2.0%Cr^{3+},*m*Si.

Crystallogtaphic Data					
m	0.05	0.10	0.20	0.30	0.40
Lattice parameter, *a* (Å)	8.028551(21)	8.031283(67)	8.034529(17)	8.03836(12)	8.037022(30)
Volume($Å^3$)	517.5014(40)	518.030(13)	518.6582(33)	519.400(23)	519.1413(57)
R_{wp}	0.051	0.054	0.058	0.113	0.070
R_p	0.038	0.040	0.044	0.083	0.051
Gof	1.61	1.74	1.80	1.74	2.25
Site occupancy fractions:					
Mg (1/8, 1/8, 1/8)	0.250	0.225	0.125	0.772	0.559
Al (1/8, 1/8, 1/8)	0.700	0.625	0.675	0.108	0.061
Si (1/8, 1/8, 1/8)	0.050	0.100	0.200	0.120	0.400
Mg (1/2, 1/2, 1/2)	0.375	0.387	0.438	0.114	0.010
Al (1/2, 1/2, 1/2)	0.615	0.603	0.553	0.876	0.980
Cr(1/2, 1/2, 1/2)	0.010	0.010	0.010	0.010	0.010
Isotropic temperature factor, Biso:					
Mg/Al(1/8,1/8,1/8)	0.729(37)	0.581(39)	0.920(44)	0.200(36)	0.699(36)
Al/Mg(1/2,1/2,1/2)	1.742(50)	1.395(52)	1.796(58)	0.444(36)	1.491(36)
O (*u*, *u*, *u*)	0.200(96)	0.200(11)	0.380(12)	0.371(36)	0.200(36)

Table S20 IQE, AE, and EQE values of $MA_{3.5}S$:2.0%Cr^{3+},*m*Si.

m	IQE (%)	AE (%)	EQE (%)
0.00	95	35	33
0.05	94	40	38
0.10	94	46	43
0.20	95	52	49
0.30	94	55	52
0.40	90	54	49

Table S21 The total elastic moduli (kBar) of $MA_{1.75}S$:2.0%Cr^{3+},0.3Si (Θ_D = 833.5 K).

Direction	XX	YY	ZZ	XY	YZ	ZX
XX	2742.4939	1041.4702	1033.6552	101.4221	153.7186	-28.0104
YY	1041.4702	2960.3784	1019.3803	138.8917	46.4304	-108.7923
ZZ	1033.6552	1019.3803	2714.7605	187.3961	49.3729	-35.8546
XY	101.4221	138.8917	187.3961	1132.6064	29.2517	55.6608
YZ	153.7186	46.4304	49.3729	29.2517	1208.1090	79.8732
ZX	-28.0104	-108.7923	-35.8546	55.6608	79.8732	1235.9351

Table S22 EXAFS fitting parameters at the Cr *K*-edge for samples. (S_0^2=0.7)

Sample	Path	N^a	R(Å)^b	σ^2(Å^2)^c	ΔE_0(eV)^d	R factor
Cr foil	Cr-Cr1	8.00	2.49	0.0068	3.48	0.0378
	Cr-Cr2	6.00	2.86	0.0050	3.48	
CrO_2	Cr-O1	2.00	1.77	0.0124	-8.41	0.0122
	Cr-O2	4.20	1.93	0.0087	-5.21	
Cr_2O_3	Cr-O1	3.00	1.95	0.0053	-3.20	0.0183
	Cr-O2	3.00	2.00	0.0029	-9.05	
$MA_{2.0}S$:2.0%Cr^{3+}	Cr-O	5.64	1.98	0.0030	-8.55	0.0132
$MA_{3.5}S$:2.0%Cr^{3+}	Cr-O1	3.00	1.71	0.0052	-7.19	0.0163
	Cr-O2	3.00	1.97	0.0003	-7.19	
$MA_{3.5}S$:2.0%Cr^{3+},0.30Si	Cr-O1	3.07	1.67	0.0138	-8.11	0.0128
	Cr-O2	3.21	1.96	0.0015	-8.11	

[a]*CN*, coordination number; [b]*R*, distance between absorber and backscatter atoms; [c]σ^2, Debye-Waller factor to account for both thermal and structural disorders; [d]ΔE_0, inner potential correction; *R* factor indicates the goodness of the fit. According to the experimental EXAFS fit of

Cr foil by fixing *CN* as the known crystallographic value.

Fitting range: 3.0 ≤ *k* (/Å) ≤ 12.5 and 1.5 ≤ *R* (Å) ≤ 3.5 (Cr foil); 3.0≤ *k* (/Å) ≤ 9.4; 3.0 ≤ *k* (/Å) ≤ 10.4 and 1.0 ≤ *R* (Å) ≤ 2.3 (Cr_2O_3); 3.0 ≤ *k* (/Å) ≤ 12.3 and 1.0 ≤ *R* (Å) ≤ 2.5 ($MA_{2.0}$: 2%Cr^{3+}); 3.0 ≤ *k* (/Å) ≤ 11.0 and 1.0 ≤ *R* (Å) ≤ 1.9 ($MA_{3.5}$: 2%Cr^{3+}); 2.8≤ *k* (/Å) ≤ 10.2 and 1.0 ≤ *R* (Å) ≤ 2.0 ($MA_{3.5}S_{0.3}$: 2%Cr^{3+}). The four parameters, coordination number, bond length, Debye-Waller factor and E_0 shift (*CN*, *R*, σ^2, ΔE_0) were fitted and partially fixed.

Table S23 Comparison of PL properties, price, device efficiency with the reported works. Note that the price mentioned here only approximately estimates the cost of the raw materials for these phosphors, and the device efficiency (η) was the NIR photoelectric efficiency of the corresponding pc-LED device at the rated current (or the maximum current used).

Phosphors	Price	λ_{PL} (nm)	IQE (%)	FWHM (nm)	$I_{150°C}$ (%)	η (%)	Ref.
$MA_{1.75}S$:2.0%Cr^{3+},0.3Si	low	850	94	265	77	16	This work
$MA_{1.75}S$:1.0%Cr^{3+},0.3Si	low	828	96	281	81	/	This work
$K_3LuSi_2O_7$:Eu^{2+}	high	740	15	160	59	7	1
$Sr_3Li_4Si_2N_6$:Eu^{2+}	high	800	30	150	/	7	2
$MgAlGa_{0.7}B_{0.3}O_4$:Cr^{3+}	middle	800	94	260	85	6	7
CaS:Eu^{2+}-Tb^{3+}	middle	810	10	195	< 50	2	3
La_2MgZrO_6:Cr^{3+}	middle	825	58	210	53	/	4
$GaTaO_4$:Cr^{3+}	high	840	91	140	60	4	5
$Mg_4Ta_2O_9$:Cr^{3+}	middle	842	87	167	30	10	6
$MgAlGa_{0.7}B_{0.3}O_4$:Cr^{3+}	middle	800	94	260	85	6	7
$La_3Ga_5GeO_{14}$:Cr^{3+}	middle	850	30	330	90	2	8
$Mg_{1.2}Ga_{1.8}O_{3.8}F_{0.2}$:$Cr^{3+}$	middle	870	93	215	85	9	9
$LiScGe_2O_6$:Cr^{3+}	high	886	73	160	37	9	10
$NaScGe_2O_6$:Cr^{3+}	high	895	40	162	20	1	11
Ca_2InSbO_6:Fe^{3+}	middle	935	87	146	18	< 1	12
$CaSc_{0.85}Al_{1.15}SiO_6$:$Cr^{3+}$	middle	950	30	205	50	/	13
$LiIn_2SbO_6$:Cr^{3+}	high	970	7	225	2	< 1	14
$LiScGeO_4$:Cr^{3+}	high	1120	26	300	13	< 1	15

References

1. Qiao, J. W., Zhou, G. J., Zhou, Y. Y., Zhang, Q. Y. & Xia, Z. G. Divalent europium-doped near-infrared-emitting phosphor for light-emitting diodes. *Nat. Commun.* **10**, 5267 (2019).

2. Li, S. X., Amachraa, M., Chen, C., Wang, L., Wang, Z. B., Ong, S. P. *et al.* Efficient near-infrared phosphors discovered by parametrizing the Eu(II) 5d-to-4f energy gap. *Matter* **5**, 1924-1936 (2022).

3. Joos, J.J., Van der Heggen, D., Martin, L.I.D.J. *et al.* Broadband infrared LEDs based on europium-to-terbium charge transfer luminescence. *Nat. Commun.* **11**, 3647 (2020).

4. Zeng, H. T., Zhou, T. L., Wang, L. & Xie, R. J. Two-Site Occupation for Exploring Ultra-Broadband Near-Infrared Phosphor-Double-Perovskite $La_2MgZrO_6:Cr^{3+}$. *Chem. Mater.* **31**, 5245-5253 (2019).

5. Zhong, J. Y., Zhuo, Y., Du, F., Zhang, H. S., Zhao, W. R., You, S. H. *et al.* Efficient Broadband Near-Infrared Emission in the $GaTaO_4:Cr^{3+}$ Phosphor. *Adv. Opt. Mater.* **10**, 2101800 (2022).

6. S. Wang, R. Pang, T. Tan, H. Wu, *et al.* Achieving High Quantum Efficiency Broadband NIR $Mg_4Ta_2O_9:Cr^{3+}$ Phosphor Through Lithium-Ion Compensation. *Adv. Mater.* **35**, 2300124 (2023).

7. C. Zhong, Y. Xu, X. Wu, S. Yin, *et al.* High Output Power and High Quantum Efficiency in Novel NIR Phosphor $MgAlGa_{0.7}B_{0.3}O_4:Cr^{3+}$ with Profound FWHM Variation. *Adv. Mater.* 36, 2309500 (2024).

8. Rajendran, V., Fang, M.-H., Guzman, G. N. D., Lesniewski, T., Mahlik, S., Grinberg, M. *et al.* Super Broadband Near-Infrared Phosphors with High Radiant Flux as Future Light Sources for Spectroscopy Applications. *ACS Energy Lett.* **3**, 2679-2684 (2018).

9. L. Yao, Q. Jia, S. Yu, C. Liang, *et al.* Simultaneous Absorption and Near-Infrared Emission Enhancement of Cr^{3+} Ions in $MgGa_2O_4$ Spinel Oxide via Anionic F-Substitution. *Adv. Optical Mater.* **11**, 2202458 (2023).

10. Chen, X. H., Song, E. H., Zhou, Y. Y., He, F. Q., Yang, J. Q. & Zhang, Q. Y. Distorted octahedral site occupation-induced high-efficiency broadband near-infrared emission in $LiScGe_2O_6:Cr^{3+}$ phosphor. *J. Mater. Chem. C* **9**, 13640-13646 (2021).

11. Zhou, X. F., Geng, W. Y., Li, J. Y., Wang, Y. C., Ding, J. Y. & Wang, Y. h. An Ultraviolet-Visible and Near-Infrared-Responded Broadband NIR Phosphor and Its NIR Spectroscopy Application. *Adv. Opt. Mater.* **8**, 1902003 (2020).

12. Liu, D. J., Li, G. G., Dang, P. P., Zhang, Q. Q., Wei, Y., Qiu, L. *et al.* Highly efficient Fe^{3+}-doped $A_2BB'O_6$ (A = Sr^{2+}, Ca^{2+}; B, B′ = In^{3+}, Sb^{5+}, Sn^{4+}) broadband near-infrared-emitting phosphors for spectroscopic analysis. *Light Sci. Appl.* **11**, 112 (2022).

13. Liu, G. C., Molokeev, M. S. & Xia, Z. G. Structural Rigidity Control toward Cr^{3+}-Based Broadband Near-Infrared Luminescence with Enhanced Thermal Stability. *Chem. Mater.* **34**, 1376-1384 (2022).

14. Liu, D. J., Li, G. G., Dang, P. P., Zhang, Q. Q., Wei, Y., Lian, H. Z. *et al.* Simultaneous Broadening and Enhancement of Cr^{3+} Photoluminescence in $LiIn_2SbO_6$ by Chemical Unit Cosubstitution: Night-Vision and Near-Infrared Spectroscopy Detection Applications. *Angew. Chem. Int. Ed. Engl.* **60**, 14644-14649 (2021).

15. Miao, S. H., Liang, Y. J., Zhang, Y., Chen, D. X. & Wang, X. J. Broadband Short-Wave Infrared Light-Emitting Diodes Based on Cr^{3+}-Doped $LiScGeO_4$ Phosphor. *ACS Appl. Mater. Interfaces* **13**, 36011-36019 (2021).